# Hydrodynamical backflow in X-shaped radio galaxy PKS 2014−55

W. D. Cotton,[1,2]★ K. Thorat,[3] J. J. Condon,[1]★ B. S. Frank,[2,4,5] G. I. G. Józsa,[2,6,7]
S. V. White [6] R. Deane [3] N. Oozeer,[2,8] M. Atemkeng,[9] L. Bester,[2,6] B. Fanaroff,[2]
R. S. Kupa,[2,6] O. M. Smirnov,[2,6] T. Mauch,[2] V. Krishnan[2] and F. Camilo[2]

[1]*National Radio Astronomy Observatory, 520 Edgemont Road, Charlottesville, VA 22903, USA*
[2]*South African Radio Astronomy Observatory, 2 Fir St, Black River Park, Observatory 7925, South Africa*
[3]*Department of Physics, University of Pretoria, Private Bag X20, Hatfield 0028, South Africa*
[4]*Department of Astronomy, University of Cape Town, Private Bag X3, Rondebosch 7701, South Africa*
[5]*Inter-University Institute for Data-Intensive Astronomy, Department of Astronomy, University of Cape Town, Private Bag X3, Rondebosch 7701, South Africa*
[6]*Department of Physics and Electronics, Rhodes University, PO Box 94, Grahamstown 6140, South Africa*
[7]*Argelander-Institut für Astronomie, Auf dem Hügel 71, D-53121 Bonn, Germany*
[8]*African Institute for Mathematical Sciences, 6 Melrose Road, Muizenberg 7945, South Africa*
[9]*Department of Mathematics, Rhodes University, PO Box 94, Grahamstown 6140, South Africa*

**ABSTRACT**

We present MeerKAT 1.28 GHz total-intensity, polarization, and spectral-index images covering the giant (projected length $l \approx 1.57$ Mpc) X-shaped radio source PKS 2014−55 with an unprecedented combination of brightness sensitivity and angular resolution. They show the clear 'double boomerang' morphology of hydrodynamical backflows from the straight main jets deflected by the large and oblique hot-gas halo of the host galaxy PGC 064440. The magnetic field orientation in PKS 2014−55 follows the flow lines from the jets through the secondary wings. The radio source is embedded in faint ($T_b \approx 0.5$ K) cocoons having the uniform brightness temperature and sharp outer edges characteristic of subsonic expansion into the ambient intragroup medium. The position angle of the much smaller ($l \sim 25$ kpc) restarted central source is within $5°$ of the main jets, ruling out models that invoke jet re-orientation or two independent jets. Compression and turbulence in the backflows probably produce the irregular and low polarization bright region behind the apex of each boomerang as well as several features in the flow with bright heads and dark tails.

**Key words:** hydrodynamics – ISM: individual objects: PGC 064440 – galaxies: active – galaxies: jets – radio continuum: galaxies – radio lines: galaxies.

## 1 INTRODUCTION

Most luminous and extended radio sources have a pair of collinear jets thought to be aligned with the spin axis of the supermassive black hole (SMBH) in the nucleus of the host galaxy (Blandford & Znajek 1977). However, 3–10 per cent are X-shaped radio galaxies (XRGs) defined by having a second set of jets or 'wings' misaligned with the first (Leahy & Williams 1984; Joshi et al. 2019). The three main models for XRGs invoke (1) a sudden or continuous reorientation of the nuclear SMBH spin axis (e.g. Ekers et al. 1978; Klein et al. 1995; Dennett-Thorpe et al. 2002),

(2) the superposition of two independent linear jets produced by two SMBHs residing in the same host galaxy (Lal & Rao 2005), or (3) hydrodynamical backflows from the overpressured main jets deflected by the ellipsoidal hot interstellar medium (ISM) of the host galaxy (e.g. Leahy & Williams 1984; Worrall, Birkinshaw & Cameron 1995; Capetti et al. 2002; Saripalli et al. 2008).

Fig. 1 is a reproduction of the prescient fig. 6a in Leahy & Williams (1984) illustrating the hydrodynamical backflow model. The nuclear SMBH (×) emits two collinear radio jets (large horizontal arrows) ending in hotspots (black dots). Hydrodynamical backflows from the ends of the jets (small horizontal arrows) initially preserve the axial symmetry of the jets. The axial symmetry is broken by the oblique hot ISM of the host galaxy (thin elliptical

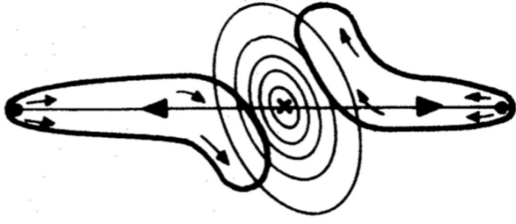★ E-mail: bcotton@nrao.edu (WDC); jcondon@nrao.edu (JJC)

**Figure 1.** This reproduction of fig. 6(a) in Leahy & Williams (1984) shows the main features of the hydrodynamical backflow model for XRGs.

contours) deflecting the backflows in opposite directions (bent arrows) and producing a radio source (heavy bent contours) with only inversion symmetry about the nucleus. Although the radio source may resemble a true XRG in low-resolution images, its actual shape is more like a double boomerang.

In this paper, we present and analyse new 1.28 GHz images of the giant XRG PKS 2014−55 (Saripalli et al. 2008; Saripalli & Subrahmanyan 2009) based on data from the recently completed 64-element MeerKAT array of the South African Radio Astronomy Observatory (SARAO) in the Northern Cape of South Africa. We show that the morphology, spectrum, and magnetic field structure of this source are very consistent with the hydrodynamical model and are inconsistent with other proposed models for X shaped sources. The central component of PKS 2014−55 = PKS 2014−558 = PKS J2018−556 (Wright & Otrupcek 1990) is identified by position coincidence with the $m_v \approx 15.5$ Seyfert II elliptical galaxy PGC 064440 (Paturel et al. 1989). PGC 064440 has heliocentric redshift $z_h = 0.060\,629$ and velocity $v_h = 18176 \pm 45$ km s$^{-1}$ (Jones et al. 2009); corrected to the cosmic microwave background (CMB) frame (Fixsen et al. 1996) $z = 0.060\,252$ and $v = 18063 \pm 46$ km s$^{-1}$. All absolute quantities in this paper were calculated for a ΛCDM universe with $H_0 = 70$ km s$^{-1}$ Mpc$^{-1}$ and $\Omega_m = 0.3$ using equations in Condon & Matthews (2018). Thus PGC 064440 is at comoving distance $D_C \approx 254$ Mpc, (bolometric) luminosity distance $D_L \approx 270$ Mpc, and angular diameter distance $D_A \approx 240$ Mpc so 1 arcmin ≈ 70 kpc.

The radio observations and data reduction are described in Section 2, and the resulting images are presented in Section 3. Section 4 discusses the morphology of the radio source and its host galaxy. The data are interpreted with the asymmetric hydrodynamical model in Section 5. Our results are summarized in Section 6.

## 2 OBSERVATIONS AND DATA REDUCTION

The XRG PKS 2014−55 and its unpolarized gain/bandpass/flux-density calibrator PKS B1934−638 were observed by MeerKAT for 9.7 h on 2019 October 11 using 55 of the 64 13.5-m diameter antennas in the array. One 10 min scan on the polarization calibrator 3C 138 was also included. Additional information about MeerKAT and its specifications can be found in Jonas et al. (2016), Camilo et al. (2018), and Mauch et al. (2020). The maximum baseline length used was nearly 8 km, giving $\theta \approx 7\rlap{.}''4$ full width at half-maximum (FWHM) resolution at $\nu = 1.28$ GHz. All four correlations *XX*, *YY*, *XY*, and *YX* of the orthogonal linearly polarized feeds were divided into 4096 spectral channels of width 0.208 984 MHz. The 856 MHz total bandpass centred on 1.284 GHz includes the 1.420 GHz H I line near the $z = 0.06$ host galaxy PGC 064440 redshifted to 1.34 GHz, where the channel width is $\Delta v \approx 47$ km s$^{-1}$. The averaging time was 8 s.

### 2.1 Continuum flagging and calibration

The $(u, v)$ data were converted from the archive format to AIPS format using MeerKAT's KATDAL package.[1] The initial radio-frequency interference (RFI) flagging followed that by Mauch et al. (2020). We trimmed 144 channels from each end of the bandpass and merged the 3808 remaining spectral channels into eight spectral windows. Subsequent editing and calibration used the OBIT package (Cotton 2008).[2] In each calibration step, deviant solutions were detected and flagged along with the corresponding $(u, v)$ data. The gain/bandpass/flux-density calibrator is essentially unpolarized, so the approximation $XX = YY$ is valid. Standard structural and spectral models for PKS B1934−638 and 3C 138 were used as appropriate. Our flux-density scale is based on the Reynolds (1994) polynomial fit for the spectrum of PKS B1934−638:

$$\log(S) = -30.7667 + 26.4908 \log\left(\frac{\nu}{\text{MHz}}\right)$$
$$- 7.0977 \log\left(\frac{\nu}{\text{MHz}}\right)^2 + 0.605\,334 \log\left(\frac{\nu}{\text{MHz}}\right)^3, \quad (1)$$

where $S$ is the flux density in Jy and $\nu$ is the frequency.

The main flagging and calibration steps were:

(i) **Fixed flagging:** Frequency ranges known to contain strong, persistent RFI were flagged. Projected baselines shorter than the 13.5-m dish diameter were flagged to eliminate shadowing.

(ii) **Hanning smoothing:** The spectral channels were Hanning smoothed (channel weights 1/4, 1/2, 1/4) to reduce possible Gibbs ringing from strong narrow band RFI. This doubled the effective channel bandwidth.

(iii) **Initial flagging:** Running medians in time and frequency were compared with the data to reveal variable and/or narrow band RFI for flagging.

(iv) **Initial *X–Y* phase calibration:** Cross-hand phase corrections were determined from the noise diode calibration signals injected into each data stream at the beginning of the observing session.

(v) **Delay calibration:** Residual group delays were determined from PKS B1934−638.

(vi) **Bandpass calibration:** Amplitude and phase correction spectra were determined from PKS B1934−638.

(vii) **Amplitude and phase calibration:** Complex gain solutions for PKS B1934−638 were determined and applied to the target field.

(viii) **Flagging of calibrated data:** Flagging operations for which calibrated data are needed were done.

(ix) **Repeat:** Flags from the steps (i)–(viii) were kept and the calibration steps (iv)–(viii) were repeated.

(x) **Polarization calibration:** After a further averaging of two spectral channels, instrumental polarization was determined from the unpolarized calibrator PKS B1934−638; solutions were obtained in 14.2-MHz blocks. The cross-hand delay and phase were determined from the polarized calibrator 3C 138. All polarization calibration parameters, including feed orientation, were determined jointly in a non-linear least squares solution using all calibrators.

Finally, the calibrated $(u, v)$ data were averaged in time to reduce their volume. The averaging times were subject to the baseline-dependent constraint that averaging reduce the amplitudes by ≤1 per cent inside the circle of radius $\rho = 1\rlap{.}°2$ centred on the target, and they never exceeded 30 s.

[1] https://libraries.io/github/ska-sa/katdal
[2] http://www.cv.nrao.edu/~bcotton/Obit.html

## 2.2 Continuum imaging

The continuum imaging used the OBIT task MFIMAGE, which was described in more detail by Cotton et al. (2018). The non-coplanar array in our extended synthesis was corrected by covering the imaged sky with small tangential facets out to radius $\rho = 1°2$ and placing additional facets on outlying sources stronger than $S \approx 6$ mJy from the 843 MHz SUMSS catalogue (Mauch et al. 2003). Variations of sky brightness and antenna gain across our wide bandpass were accommodated by dividing the observed spectrum into 34 frequency bins having ∼2 per cent fractional bandwidths. The frequency bins were imaged independently and CLEANed jointly. Three iterations of phase self-calibration were applied. The CLEAN window was mostly generated automatically, but with some manual assistance to cover all of the extended emission. The multiresolution Stokes I CLEAN used 1032 004 components, a 3 per cent loop gain, and included 3.394 Jy of total flux density after CLEANing to a depth of 15 μJy beam$^{-1}$. Spectra were least-squares fitted in each pixel using frequency bin weights inversely proportional to the square of the image-plane rms noise.

Stokes Q and U were imaged out to a radius $\rho = 1°0$ and CLEANed for 50 000 components to a depth of 28 μJy beam$^{-1}$ in Stokes Q and 15 μJy beam$^{-1}$ in Stokes U. Rotation measures (RMs) and electric-vector polarization angles (EVPAs) corrected to zero wavelength for each pixel were derived by a search in RM space, essentially taking the peak of the rotation measure synthesis function Brentjens & de Bruyn (2005). The RM that gave the highest polarized intensity in the average RM-corrected value of the $P = \sqrt{Q^2 + U^2}$ was taken as the RM, the peak average $P$ as the polarized intensity, and the polarization angle of the RM-corrected average $Q + iU$ as the EVPA at zero wavelength. The EVPA at zero wavelength is orthogonal to the source magnetic field vector $B$ integrated through the source. There is little evidence for effects beyond a simple well-resolved, external Faraday screen. The fractional polarization image was derived by first correcting the frequency averaged polarized intensity for the Ricean bias and dividing by the frequency averaged total intensity.

## 2.3 Continuum spectral index

The imaging described in Section 2.2 used tapering in the outer portion of the $(u, v)$ plane to minimize the variation of resolution with frequency but did not address a similar problem in the inner portion of the $(u, v)$ plane that distorts the spectral-index image. Further imaging similar to that described in Section 2.2 was done using a Gaussian taper in the inner $(u, v)$ plane with rms length $\sigma = 500\lambda$ to reduce the frequency dependence of the short-baseline coverage. In order to better explore the faintest emission, we convolved the images of the individual frequency planes to $\theta_{1/2} = 15$ arcsec before making frequency-dependent primary beam corrections and fitting for the spectral index.

## 2.4 Spectral-line calibration and imaging

The 1420 MHz H I line frequency at the redshift $z = 0.06$ of PGC 064440 is 1340 MHz. We reduced a 50 MHz subset of the visibility data including this frequency using the IDIA Pipeline[3] to produce a spectroscopic data cube containing the H I line around PGC 064440. The IDIA pipeline is based entirely on CASA (McMullin et al. 2007) tasks. The basic workflow follows the calibration

[3]https://www.idia-pipelines.github.io

process described above. After the continuum subtraction using CASA's UVCONTSUB task to fit a polynomial to the visibility spectra, we used CASA's TCLEAN task with the widefield gridder performing 1000 CLEAN iterations per channel. A Briggs weighting with robust = 0.5 was used to optimize the shape of the dirty beam while minimizing sensitivity loss. We measured the image noise to be $\sigma \sim 125$ μJy beam$^{-1}$. The FWHM resolution in the H I cube is $\theta = 19''2 \times 17''6$.

# 3 THE RADIO IMAGES

## 3.1 Total intensity continuum

UnCLEANed flux from the very extended radio source PKS 2014−55 and background sources in the primary beam, combined with the lack of projected baselines shorter than the 13.5-m antenna diameter, left a wide but very shallow negative 'bowl' in the total-intensity image. We used the AIPS task IMEAN to measure the mode of the intensity distribution of pixels in source-free areas near PKS 2014−55; it is $-4.6 \pm 1.0$ μJy beam$^{-1}$. To fill in the bowl, we added 4.6 μJy beam$^{-1}$ to the image zero level. We divided this image by the circularized 67 arcmin FWHM primary beam attenuation pattern specified by Mauch et al. (2020) equations (3) and (4) to yield the final 'sky' image shown in Fig. 2. The actual primary beam is slightly elliptical with axial ratio $a/b \approx 1.04$ and rotates with parallactic angle on the sky. However, the maximum attenuation error introduced by our circular approximation is a negligible <0.3 per cent even at the ends of PKS 2014−55, $\rho = 12$ arcmin from the pointing centre.

The image was restored with a $7''43 \times 7''35$ Gaussian beam, so the brightness temperature corresponding to a spectral intensity $S_p = 1$ μJy beam$^{-1}$ is $T_b \approx 13.7$ mK at $\nu = 1.28$ GHz. The rms noise plus confusion is $\sigma = 3.5 \pm 0.2$ μJy beam$^{-1}$.

We used the AIPS task TVSTAT to measure the total 1.28 GHz flux density in the $\Omega = 1.02 \times 10^{-5}$ sr region bounded by the faint 'cocoon' that makes Fig. 2 resemble the photograph of a jellyfish; it is $S = 2.36 \pm 0.08$ Jy, with the quoted error being dominated by an estimated 3 per cent uncertainty in the absolute flux-density scale. Inside the region subtended by PKS 2014−55, the $4.6 \times 10^{-6}$ Jy beam$^{-1}$ bowl correction contributed only $S \approx 0.03$ Jy to the total flux density. The smooth bowl correction is only ∼12 per cent of the average cocoon brightness, so our detection of the sharp-edge cocoons is quite reliable. Most published flux densities (e.g. Wright & Otrupcek 1990; Hindson et al. 2014) at nearby frequencies appear to be about 25 per cent lower than ours, perhaps because they did not capture the full extent of this very large source. The Murchison Widefield Array (MWA) flux densities (Hindson et al. 2014) $S = 15.2 \pm 0.8$, $13.3 \pm 0.7$, $11.3 \pm 0.6$, and $8.8 \pm 0.5$ Jy at 120, 149, 180, and 226 MHz, respectively, are consistent with PKS 2014−55 having an overall spectral index $\alpha \equiv +$dln $S$/dln $\nu$ in the range $-1.0 < \alpha < -0.8$.

The central region in our 1.28 GHz total-intensity image of PKS 2014−55 (Fig. 3) is well fit by the sum of three Gaussian components: two with completely free size and position parameters plus a (forced) point source with free position and flux density representing a possible radio core between them. The results are listed in Table 1. Although it is not clearly visible in Fig. 3, the $32 \pm 6$ mJy core component is required for the best fit and its fitted position is <1 arcsec from the nucleus of the host galaxy PGC 064440. The line connecting the two outer components has position angle $PA = 154°$ measured from north to east.

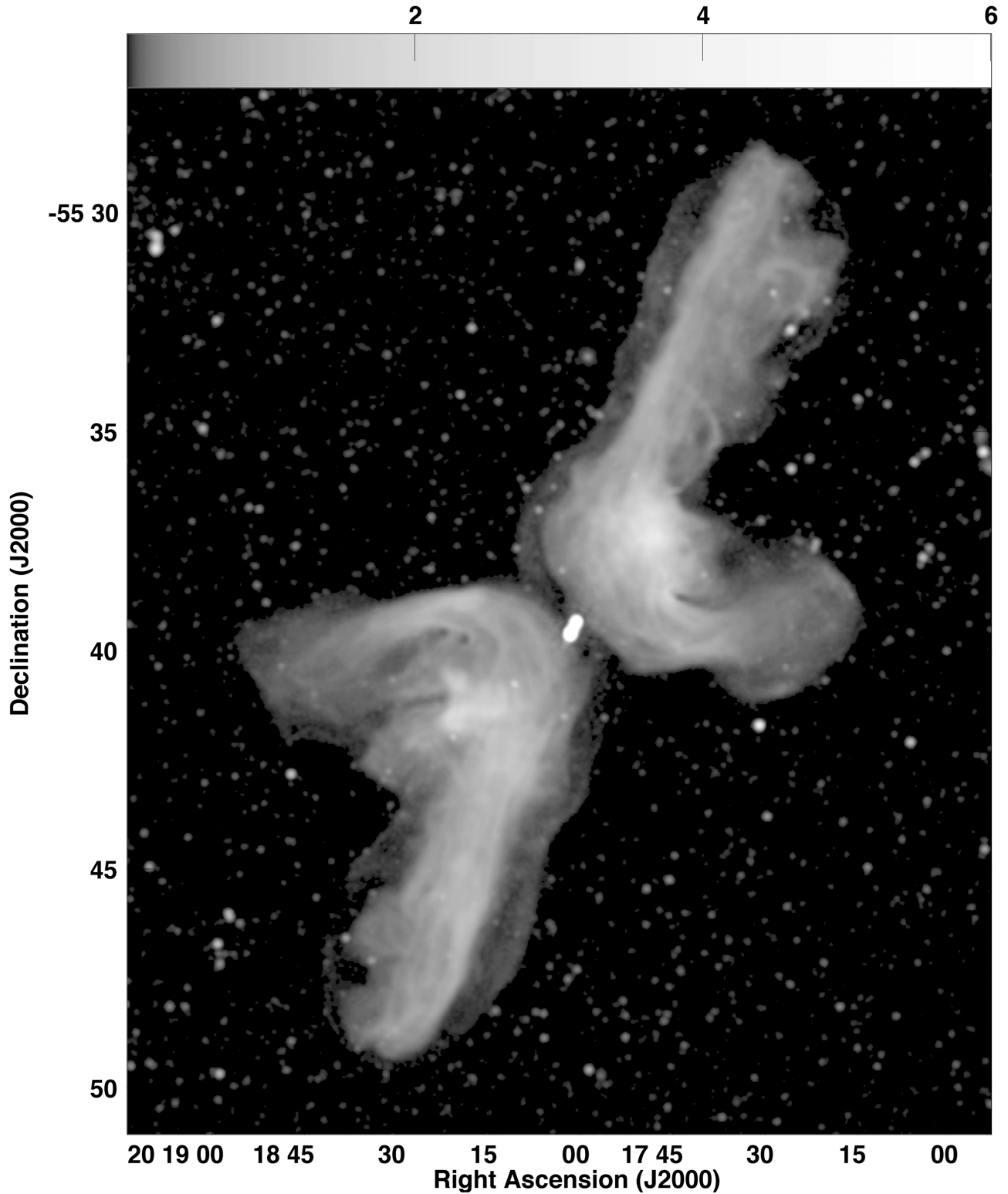**Figure 2.** This 1.28 GHz MeerKAT 'sky' image of PKS 2014−55 was restored with a $\theta_{1/2} \approx 7\rlap{.}''4 \approx 8.6$ kpc FWHM Gaussian beam, corrected for the $-4.6 \pm 1.0$ µJy beam$^{-1}$ bowl, and divided by the primary attenuation pattern. The rms noise plus confusion is $\sigma = 3.5 \pm 0.2$ µJy beam$^{-1}$ = 48 ± 3 mK. The logarithmic grey scale spans 0.006–6 mJy beam$^{-1}$ (grey-scale bar at top) to reveal the extremely faint ($T_b \sim 0.5$ K) radio cocoons most conspicuous on the east side of the northern arm and on the west side of the southern arm. The bright central region is completely saturated, but it is accurately represented by the contour map in Fig. 3.
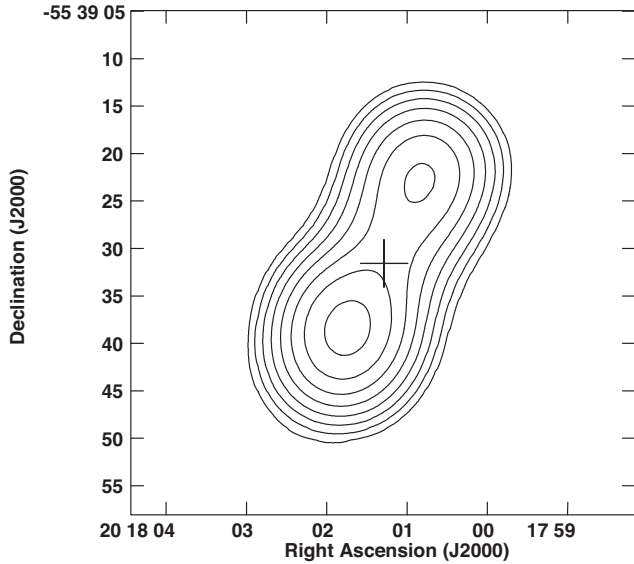
**Figure 3.** The bright central region of PKS 2014−55 at 1.28 GHz is represented by contours at $1\,\mathrm{mJy\,beam^{-1}} \times 2^0, 2^1, 2^2, \ldots, 2^7$. The cross marks the accurate position J2000 $\alpha = 20^\mathrm{h}\,18^\mathrm{m}\,01\overset{\mathrm{s}}{.}286$, $\delta = -55°\,39'\,31\overset{''}{.}59$ (Skrutskie et al. 2006) of the near-infrared source 2MASX J201801.27−553931.5 identified with PGC 064440.

**Table 1.** The positions, 1.28 GHz flux densities, deconvolved major and minor diameters between half-maximum points, and major-axis position angles of Gaussian fits to the central region of PKS 2014−55.

| J2000 | | $S$ | $\phi_\mathrm{M} \times \phi_\mathrm{m}$ (arcsec × arcsec) | $PA$ |
|---|---|---|---|---|
| $\alpha$ | $\delta$ | (mJy) | | (deg) |
| $20^\mathrm{h}\,18^\mathrm{m}\,00\overset{\mathrm{s}}{.}84$ | $-55°\,39'\,22\overset{''}{.}9$ | 88 | $5.2 \times 1.4$ | 159 |
| $20^\mathrm{h}\,18^\mathrm{m}\,01\overset{\mathrm{s}}{.}2$ | $-55°\,39'\,31''$ | $32 \pm 6$ | $0 \times 0$ | ... |
| $20^\mathrm{h}\,18^\mathrm{m}\,01\overset{\mathrm{s}}{.}74$ | $-55°\,39'\,38\overset{''}{.}5$ | 211 | $5.4 \times 1.1$ | 154 |

Saripalli et al. (2008) imaged the central region of PKS 2014−55 with sub-arcsec resolution and found five nearly collinear radio components: a central core, an inner double source, and an outer double source. The position angles of their inner and outer doubles are $+150°$ and $+156°$, respectively. Thus each long, narrow Gaussian component in Table 1 is a blend of two relatively compact sources. The Saripalli et al. (2008) radio core has a fairly flat ($\alpha > -0.5$) spectrum above $\nu = 1.28$ GHz, so it is probably synchrotron self-absorbed and completely unresolved.

### 3.2 Polarization

The rotation measure in front of PKS 2014−55 is shown in Fig. 4. It is RM $\sim 40\,\mathrm{rad\,m^{-2}}$ and varies by only a few $\mathrm{rad\,m^{-2}}$ across the source, so it may originate primarily in our Galaxy.

Polarization 'B' vectors at zero wavelength parallel to the magnetic field orientation in the emitting region are plotted as short line segments in Fig. 5. The lengths of the vectors are proportional to the fractional polarization. The magnetic vectors are nearly parallel to the main jets, as in most FR II (Fanaroff & Riley 1974) sources (Bridle et al. 1994). In contrast, the magnetic vectors are usually perpendicular to the jets in FR I sources (Bridle & Perley 1984). Fig. 5 shows that the magnetic field $B$ closely follows the apparent flow around the bends in PKS 2014−55.

The fractional polarization is high (30–50 per cent) over most of the main lobes indicating very organized magnetic fields. In the secondary lobes, the fractional polarization approaches 80 per cent indicating very little scatter in the magnetic field orientations. On the other hand, the brighter Stokes I regions at the apexes of the 'boomerangs' typically have around 15 per cent fractional polarization indicating a more tangled magnetic field structure.

### 3.3 Continuum spectral index

The spectral-index image is given in Fig. 6. The spectrum in the lobes is steep everywhere, flattening somewhat near the bright regions inside the apexes of the 'boomerangs' and becoming very steep in the cocoons and near the ends of the secondary lobes. We hesitate to provide quantitative estimates of the spectral-index errors because they are largely systematic, caused by limited sampling near the centre of the $(u, v)$ plane. Further analysis of the spectral index is being developed for a subsequent paper.

## 4 THE RADIO SOURCE PKS 2014−55 AND ITS HOST GALAXY PGC 064440

### 4.1 The radio source PKS 2014−55

The $S = 2.36\,\mathrm{Jy}$ radio source with spectral index $\alpha \approx -0.8$ has spectral luminosity $L_\nu \approx 2.0 \times 10^{25}\,\mathrm{W\,Hz^{-1}}$ at $\nu = 1.28$ GHz in the source frame. Such luminous sources (Ledlow & Owen 1996) usually have FR II morphologies (Fanaroff & Riley 1974) characterized by narrow jets leading to hotspots in edge-brightened lobes. PKS 2014−55 does not (Fig. 2); its long, filamentary, and diffuse main 'jets' are only decaying relics of activity that ceased millions of years ago. Saripalli & Subrahmanyan (2009) found several examples of XRGs lacking hotspots at the ends of their relic jets and noted that the current lack of hotspots cannot be used to rule out backflows from earlier jets that have since decayed.

The current spectral brightnesses of the relic jets are only $T_\mathrm{b} \sim 14$ K, so their minimum-energy magnetic field strengths $B_\mathrm{min}$ (e.g. Pacholczyk 1970; Worrall & Birkinshaw 2006) are low. For electrons emitting at their critical frequencies from $\nu_1 = 10^7$ to $\nu_2 = 10^{10}$ Hz, proton/electron energy ratio $\kappa$, and source line-of-sight depth $d$,

$$\left(\frac{B_\mathrm{min}}{\mu\mathrm{G}}\right) \approx 0.57\left[\left(\frac{T_\mathrm{b}}{\mathrm{K}}\right)\left(\frac{\nu(1+z)}{\mathrm{GHz}}\right)^{2-\alpha}\left(\frac{\mathrm{kpc}}{d}\right)\right]^{2/7}(1+\kappa)^{2/7} \tag{2}$$

in convenient astronomical units. Even for a line-of-sight depth $d = 100$ kpc and a high proton/electron energy ratio $\kappa = 2000$, the magnetic field strength is only $B_\mathrm{min} \sim 3\,\mu\mathrm{G}$ and the corresponding synchrotron lifetime $\tau \sim c_{12}B^{-3/2} \sim 1.3 \times 10^{16}\,\mathrm{s} \sim 4 \times 10^8$ yr (Pacholczyk 1970) is very long. The energy density of the CMB at $z = 0.06$ is the same as that of a $B \sim 3.7\,\mu\mathrm{G}$ magnetic field, so inverse–Compton (IC) scattering off the CMB reduces the radiative lifetimes in the relic jets to $\tau \sim 2 \times 10^8$ yr. The spectral steepening at the ends of the wings visible in Fig. 6 indicate ages $\tau \gtrsim 10^8$ yr. This result is typical of giant radio galaxies (Ishwara-Chandra & Saikia 1999). The minimum relativistic pressure

$$P_\mathrm{min} = \frac{13B_\mathrm{min}^2}{72\pi} \tag{3}$$

in most of PKS 2014−55 is $P_\mathrm{min} \sim 10^{-14}(1+\kappa)^{4/7}\,\mathrm{dyne\,cm^{-2}}$.

At $D_\mathrm{A} \approx 240$ Mpc, 1 arcsec $\approx 1.164$ kpc and the largest angular extent $\phi \approx 22\overset{'}{.}5$ of PKS 2014−55 implies a projected overall
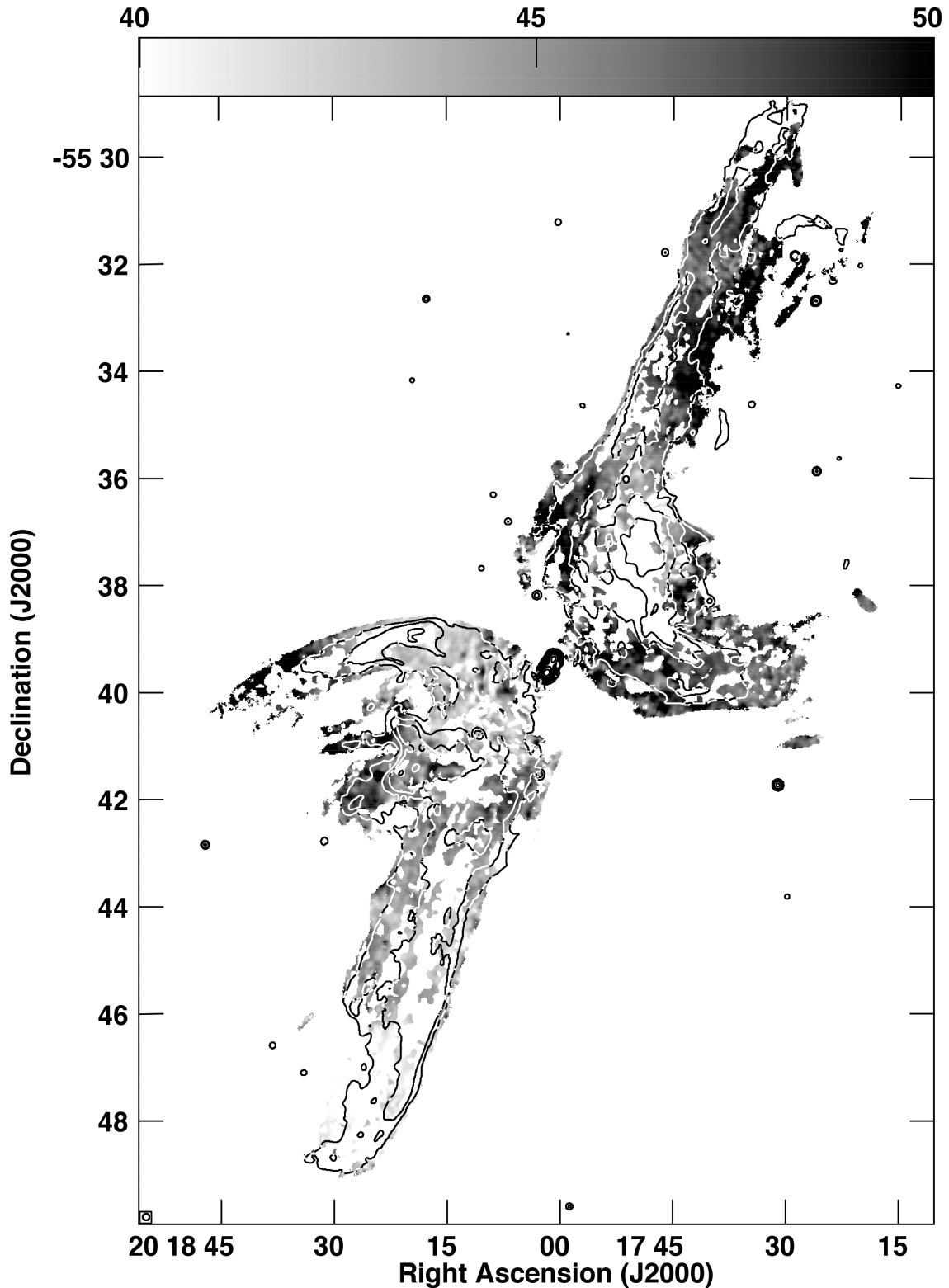
**Figure 4.** This image shows the rotation measure RM on a grey scale. The scale bar at the top has units rad m$^{-2}$. Total-intensity contours are plotted at brightnesses 100 μJy beam$^{-1}$ × 2$^0$, 2$^1$, 2$^2$, .... The $\theta_{1/2} \approx 7\rlap{.}''4$ restoring beam half-power circle is shown in the small box in the lower left corner.

length $l \approx 1.57$ Mpc. This is more than twice the traditional minimum size defining a giant radio source, $l \approx 1$ Mpc for $H_0 = 50$ km s$^{-1}$ Mpc$^{-1}$ (Willis, Strom & Wilson 1974), or $l \approx 0.7$ Mpc for $H_0 = 70$ km s$^{-1}$ Mpc$^{-1}$. Even the backflow wings

of PKS 2014−55 easily satisfy this criterion: their total projected extent is $\phi \approx 14\rlap{.}'0$ or $l \approx 0.98$ Mpc. The two long arms have nearly equal projected lengths (11$\rlap{.}'$7 and 10$\rlap{.}'$8 for the NW and SE arms, respectively) and flux densities (1.033 and 1.025 Jy),
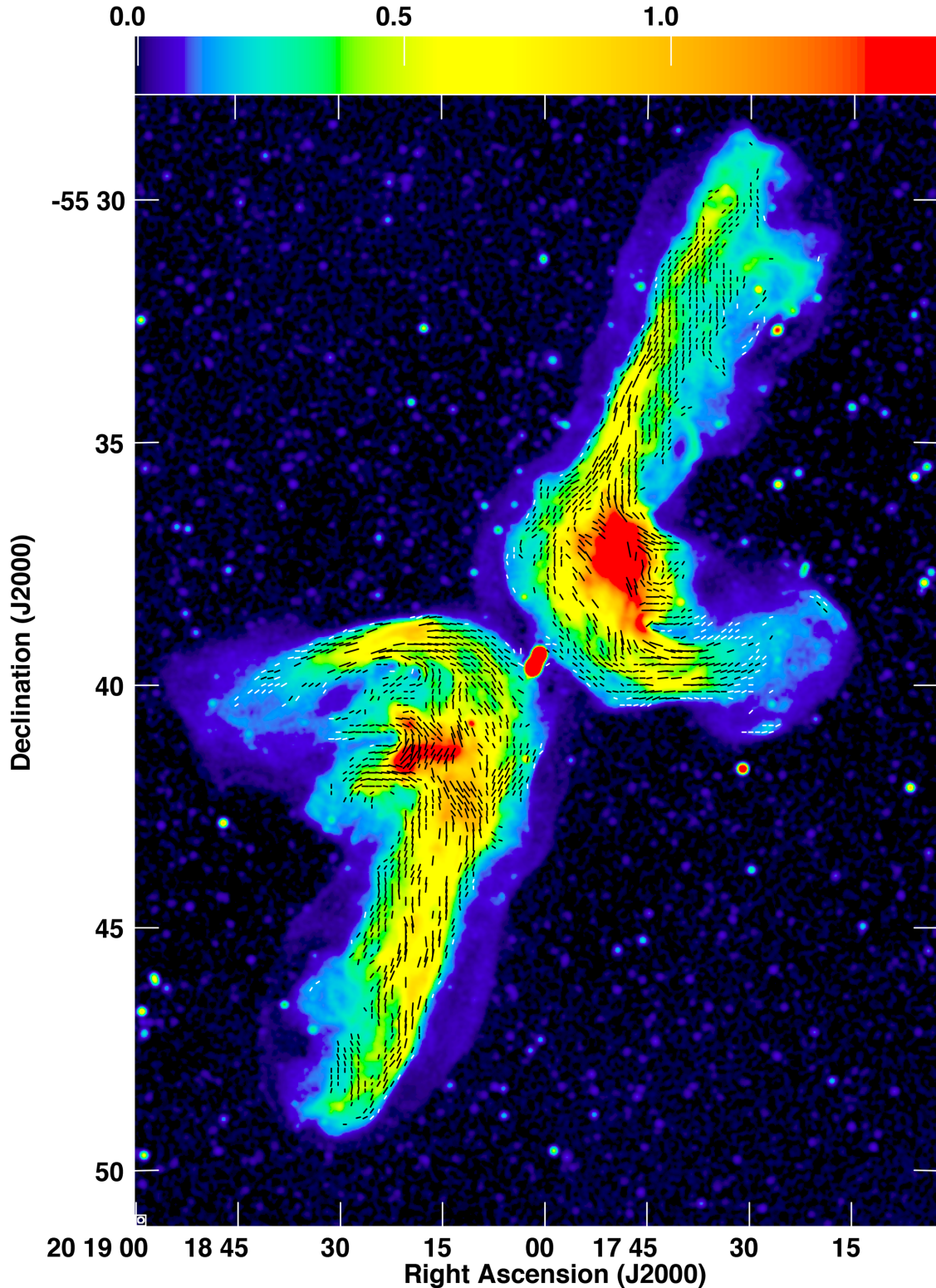
**Figure 5.** The black and white lines are parallel to $B$ and have length 1 arcsec per $P = 4.2$ per cent fractional polarization. The colour bar gives the linear total-intensity scale between $-0.005$ and $1.5\,\mathrm{mJy\,beam^{-1}}$. The $\theta_{1/2} \approx 7\!''\!.4$ restoring beam half-power circle is shown in the small box in the lower left corner.

so they show no evidence for relativistic time delays or flux boosting.

PKS 2014−55 extends far beyond the virial radius of its host galaxy and directly probes the ambient intergalactic medium (IGM).

PGC 064440 is not in a cluster environment rich enough to have a significant intracluster medium. Malarecki et al. (2015) made a spectroscopic study of the Mpc-scale environments for a sample of low-redshift giant radio galaxies including PKS 2014−55. The
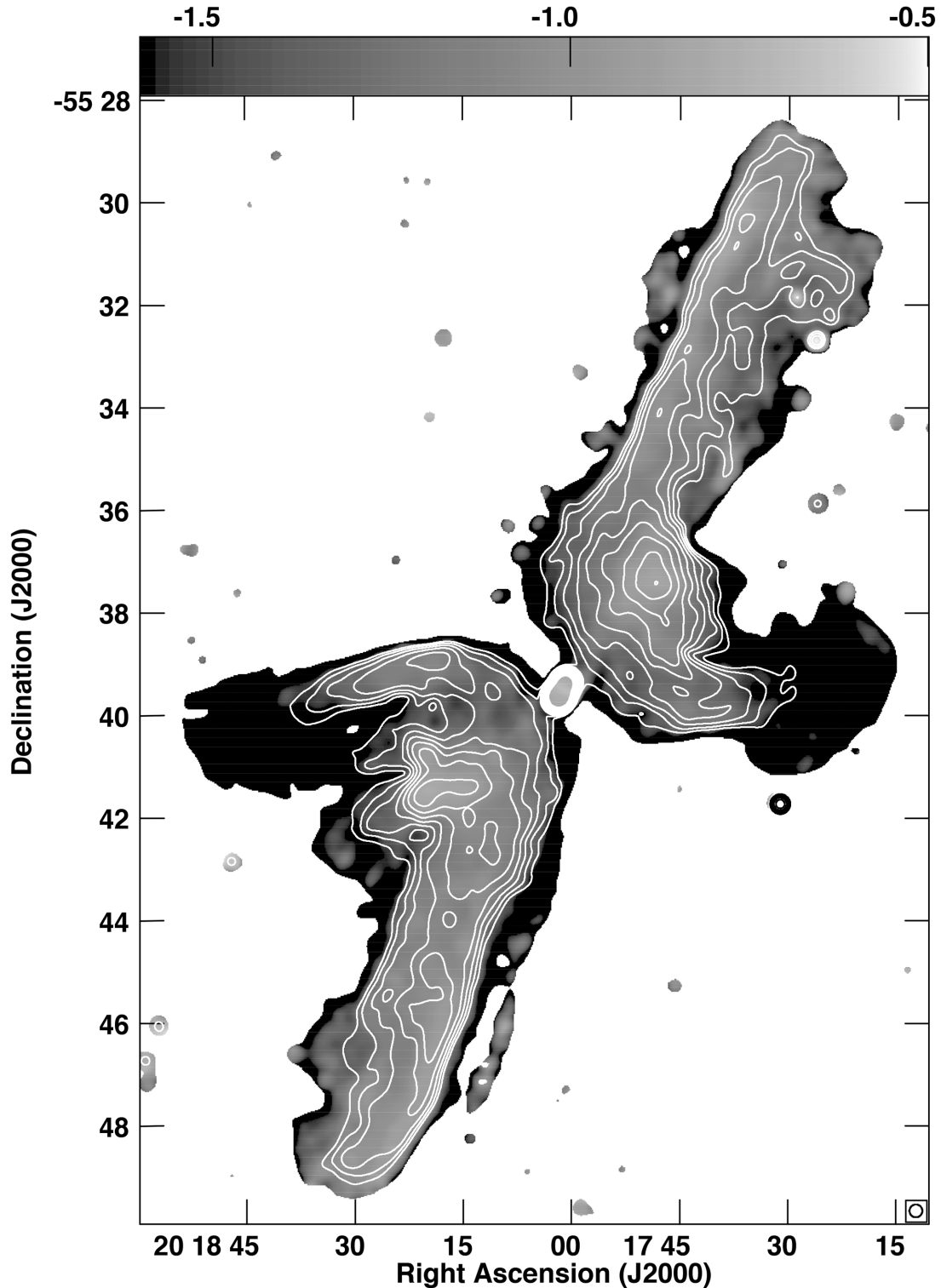
**Figure 6.** The grey scale image shows the spectral index $\alpha$ with values given by the scale bar at the top. The white contours mark total intensities $0.5\,\mathrm{mJy\,beam^{-1}} \times 2^0,\ 2^{1/2},\ 2^1 \ldots$. The 15 arcsec half-power circle is drawn inside the small box at the lower right.

number density of galaxies more luminous than $-19.49$ mag in a cylinder of 1 Mpc radius and 24 Mpc length along the line-of-sight centred on PKS 2014−55 is only $n \sim 0.066\,\mathrm{Mpc^{-3}}$, a typical density in galaxy groups and poor clusters, but a factor of 10 lower than in galaxy clusters.

The faint radio cocoons in Fig. 7 are defined by their fairly constant brightness temperatures $T_\mathrm{b} \sim 0.5$ K between sharp inner and outer boundaries. Fig. 6 shows that they have the steep spectra produced by radiative losses, so, like the relic jets, they too may be relics of even earlier activity. Inserting $T_\mathrm{b} = 0.5$ K, $\nu = 1.28$ GHz,
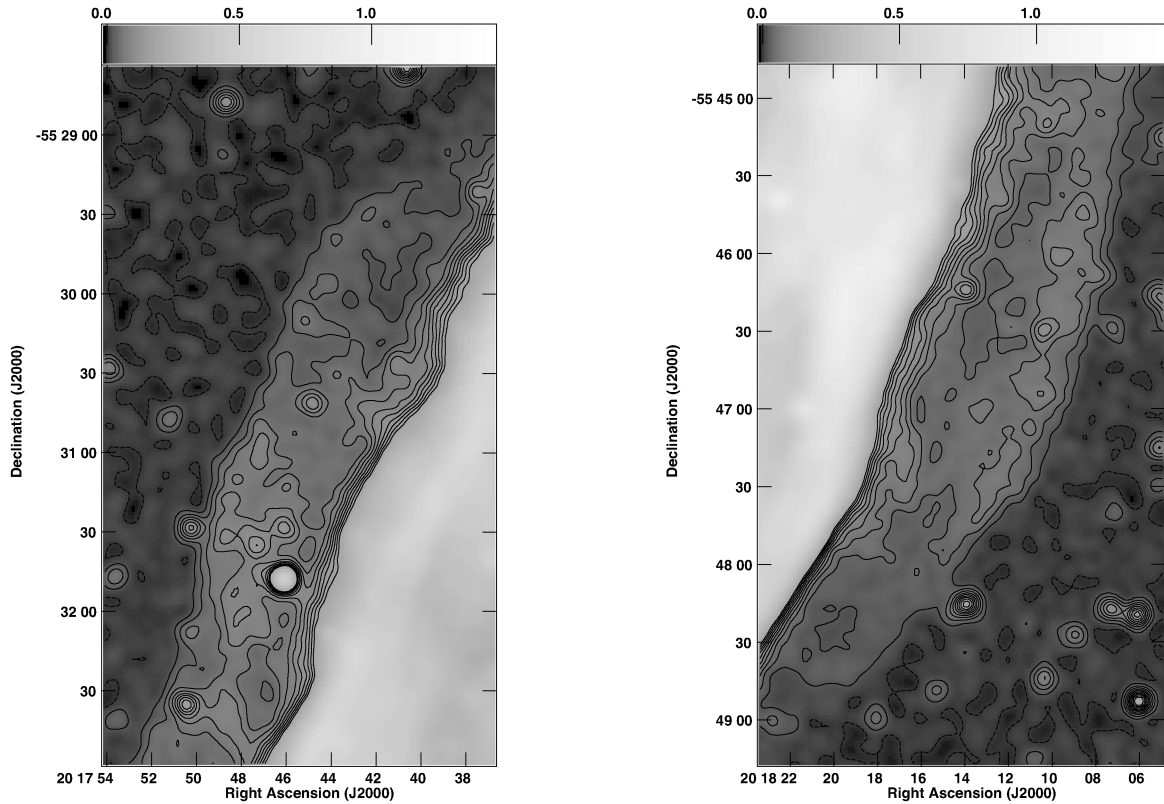
**Figure 7.** Portions of the cocoons surrounding the northern (left-hand panel) and the southern relic jets (right-hand panel) are shown with contours at $T_b = 0.25\,\mathrm{K} \times 1,\, 2,\, 3,\, \ldots,\, 10$ to emphasize their sharp inner and outer boundaries. The average brightness temperature in the cocoons is $\langle T_b \rangle \sim 0.5$ K. The logarithmic grey scale spans $-0.12\,\mathrm{K} = -0.008\,\mathrm{mJy\,beam^{-1}}$ (black) to $+20\,\mathrm{K} = +1.46\,\mathrm{mJy\,beam^{-1}}$ (white) as indicated by the scale bar at the top.

and line-of-sight depth $d = 100$ kpc into equation (2) yields $B_{\min} \approx 0.15(1+\kappa)^{2/7}\,\mu$G in the cocoon of PKS 2014−55. The corresponding magnetic energy density is $U_B \sim 1.0 \times 10^{-15}(1 + \kappa)^{4/7}$ erg cm$^{-3}$ and the minimum relativistic pressure in the cocoons is $P_{\min} \sim 1.3 \times 10^{-15}(1 + \kappa)^{4/7}$ dyne cm$^{-2}$. These low-pressure cocoons are exceptionally sensitive barometers for measuring the pressure of the intragroup medium (IGrM) or the IGM (Malarecki et al. 2013).

If the pressure $P_e$ in the external medium is less than the cocoon pressure $P_c$, the cocoon should expand laterally with speed $v_\perp$ at which the ram pressure balances the cocoon overpressure

$$v_\perp = \left( \frac{P_c - P_e}{\rho_e} \right)^{1/2},  \tag{4}$$

where $\rho_e$ is the external mass density. The IGM may contain half of all baryons and $\Omega_b \approx 0.046$, so a lower limit to the external mass density at redshift $z = 0.06$ is the mean baryonic IGM density

$$\rho_e \gtrsim \left( \frac{\Omega_b}{2} \right) \frac{3H_0^2(1+z)^3}{8\pi G} \approx 2.5 \times 10^{-31}\ \mathrm{g\ cm^{-3}}.  \tag{5}$$

For a primordial abundance of fully ionized H and He, the mean mass per particle is $\mu_e \approx 0.6 m_p \approx 1.0 \times 10^{-24}$g and the particle density is $n_e = \rho_e/\mu_e \approx 2.5 \times 10^{-7}$ cm$^{-3}$. PGC 064440 is in a poor group of galaxies, where the IGrM particle density is $\sim 10\times$ as high and the temperature range is $10^6\,\mathrm{K} < T < 10^7$ K (Stocke et al. 2019), so the external particle pressure $P_e = nkT \approx 10^{-15}$ dyne cm$^{-2}$. Even if $\kappa = 0$, the minimum cocoon pressure is comparable with the external pressure. Higher $\kappa$ or non-equipartition magnetic fields would only increase the cocoon pressure.

In the limit $P_e \ll P_c$, inserting $P_c = P_{\min}$ into equation (4) predicts that the cocoon boundary should be expanding into the surrounding medium with speeds between $v_\perp \sim 200(1+\kappa)^{2/7}$ (IGrM) and $v_\perp \sim 700(1+\kappa)^{2/7}$ km s$^{-1}$ (IGM). These expansion speeds are subsonic in the radio cocoons, allowing the cocoons enough time to reach pressure equilibrium (Begelman, Blandford & Rees 1984) and attain their constant brightness temperatures. The PKS 2014−55 cocoons are $l_\perp \approx 50$ kpc wide, so the expansion time-scales $\tau \equiv l_\perp/v_\perp$ of the cocoons are $70(1+\kappa)^{-2/7} \lesssim \tau(\mathrm{Myr}) \lesssim 250(1+\kappa)^{-2/7}$.

The energy density of the CMB surrounding PKS 2014−55 at $z = 0.06$ is $U_{\mathrm{CMB}} = 5.3 \times 10^{-13}$ erg cm$^{-3}$. It is larger than the magnetic energy density in the cocoon even in the unlikely event (Beck & Krause 2005) that $\kappa > m_p/m_e \sim 2000$. The ratio of IC losses to synchrotron losses is $U_{\mathrm{CMB}}/U_B$, so the radiative lifetimes $\sim 100$ Myr of relativistic electrons in the cocoons are strongly limited by IC scattering off the CMB, not by synchrotron radiation.

## 4.2 The host galaxy PGC 064440

The total stellar mass $M_*$ of PGC 064440 can be estimated photometrically from its $\lambda = 2.17\,\mu$m absolute magnitude $M_K$ using the empirical relation (Cappellari 2013)

$$\log_{10}(M_*/\mathrm{M}_\odot) \approx 10.58 - 0.44(M_K + 23).  \tag{6}$$

The 2MASX apparent magnitude of PGC 064440 is $m_K = 11.64$, the distance modulus is 32.16, and the $K$ correction is $K \approx 6.0\log_{10}(1 + z) \approx -0.15$ mag (Kochanek et al. 2001), so $M_K \approx -25.37$ and the total mass of stars inside the photometric radius $r \sim 34$ kpc is $\log_{10}(M_*/\mathrm{M}_\odot) \approx 11.6$.
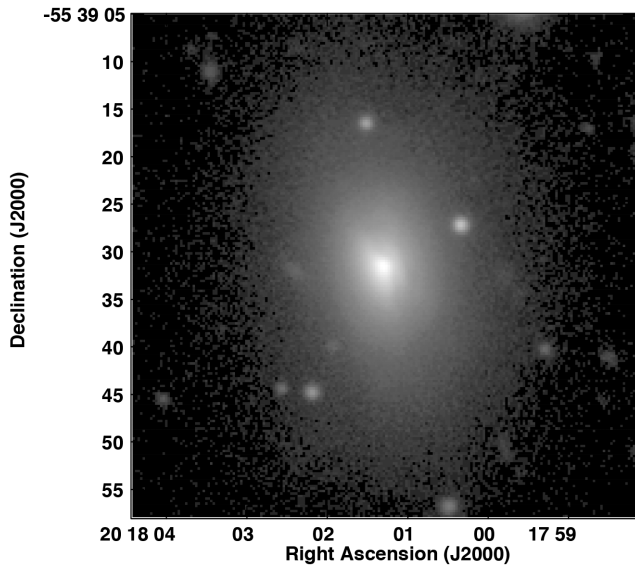
**Figure 8.** The DES DR1 *r*-band optical image of PGC064440 reveals a faint dust lane just north-west of the nucleus.

The mid-infrared source WISEA J201801.29−553931.5 (Wright et al. 2010) coincides with PGC 064440. Its mid-infrared colours $(W2 - W3) = +3.066$ and $(W1 - W2) = +1.256$ are typical of Seyfert galaxies and far from the colours of elliptical galaxies whose mid-infrared emission is dominated by stellar photospheres (Jarrett et al. 2011). This mid-infrared evidence for circumnuclear dust heated by an active galactic nucleus (AGN) is supported by the presence of a heavily obscured (column density $\log[N_H(cm^{-2})] = 23.51 \pm 0.14$) hard X-ray source at the centre of PKS 2014−55 (Panessa et al. 2016) and the absence of broad optical emission lines. Star formation may also contribute to the mid-infrared emission from PGC 064440.

PGC 064440 is a Seyfert II galaxy with very strong high-ionization ([O III]/H β ∼ 13) emission lines (Simpson et al. 1996). Many powerful radio galaxies have extended emission-line regions (EELRs) with radii $\gtrsim 100$ kpc. Tadhunter, Fosbury & Quinn (1989) observed the [O III]λ5007 line of PGC 064440 with a long slit in $PA = 192°$ nearly parallel to the continuum major axis and found emission extending ∼11 kpc on both sides of the nucleus with the linear velocity field of a constant-density enclosed mass and maximum rotation velocity $|\Delta V^{max}| \approx 280$ km s$^{-1}$ relative to the nucleus, indicating a total mass $M \sim 2 \times 10^{11}$ M$_\odot$ within ∼11 kpc of the nucleus.

# 5 THE HYDRODYNAMICAL BACKFLOW MODEL

The extended radio jets of most high-luminosity sources are linear and inversion symmetric about their host galaxies. Leahy & Williams (1984) noted that opposing axisymmetric backflows could form a fat disc expanding laterally where they encountered the hot ISM of their host galaxy, but a misaligned ellipsoidal hot gas halo could break the axial symmetry and bend the backflows in opposite directions away from the ellipsoid major axis to produce the secondary arms or 'wings' of XRGs (Fig. 1). Saripalli & Subrahmanyan (2009) found that XRGs lacking FR II hotspots often contain inner doubles, indicating restarted jets along the same axis, and they proposed that the wings are asymmetric backflows.
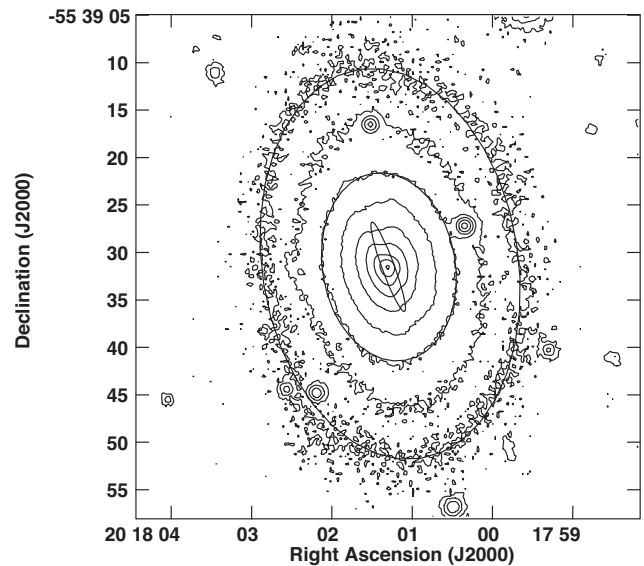


**Figure 9.** The DES *r*-band brightness contours are shown at 16 electrons × 1, 2, 4, 8, 16, 32, 64, 128, and 256. The 10 arcsec × 1″.3 ellipse in *PA* ≈ 20° at the centre represents the dust lane as a tilted ring, only the northwestern near side of which is visible in absorption.

**Table 2.** Best-fitting ellipses for the dust lane and outer brightness contours of PGC 064440.

| Ellipse | $\phi_M \times \phi_m$ (arcsec × arcsec) | $PA$ (deg) | $\cos^{-1}(\phi_m/\phi_M)$ (deg) |
|---|---|---|---|
| Dust ring | $10 \times 1.3$ | $+20$ | 82 |
| First *r* contour | $42 \times 27$ | $+9$ | 50 |
| Third *r* contour | $20 \times 14$ | $+10$ | 46 |
| $K_s$ total | $57.8 \times 41.6$ | $+15$ | 44 |

Backflows from extended radio jets can be treated as fluid flows because their magnetic fields are strong enough that even ultrarelativistic protons and electrons have Larmor radii much smaller than the jet radius. Magnetic lines of force are frozen into the jet fluid, so velocity shear across the jet tends to align the magnetic field along the jet, and jet growth can increase the frozen-in magnetic field strength to near equipartition. Many astrophysical jets are stable enough to survive bending, as demonstrated by the bent tails of radio galaxies moving through dense gas in massive galaxy clusters.

## 5.1 Backflow geometry

A faint dust lane extending ∼10 arcsec (∼ 12 kpc) is just visible in the DES DR1 (Abbott et al. 2018) *r*-band image of PGC 064440 (Fig. 8). Fig. 9 is the corresponding *r*-band brightness contour plot. The narrow inner ellipse represents the tilted circular ring that overlaps the dust lane, of which only the near half is visible in absorption. The two larger ellipses are fits to the first and third brightness contours in Fig. 9. The parameters of these ellipses and the 2MASS $K_s$ 'total' isophotal ellipse are listed in Table 2. The isophotal ellipticities $\epsilon \equiv 1 - (\phi_m/\phi_M)$ are in the range $0.28 < \epsilon < 0.36$. They indicate that PGC 064440 is an oblate ellipsoid whose equatorial position angle is $PA = 15° \pm 5°$ and whose projected polar axis is at $PA = 105° \pm 5°$. If the dust lane is an equatorial

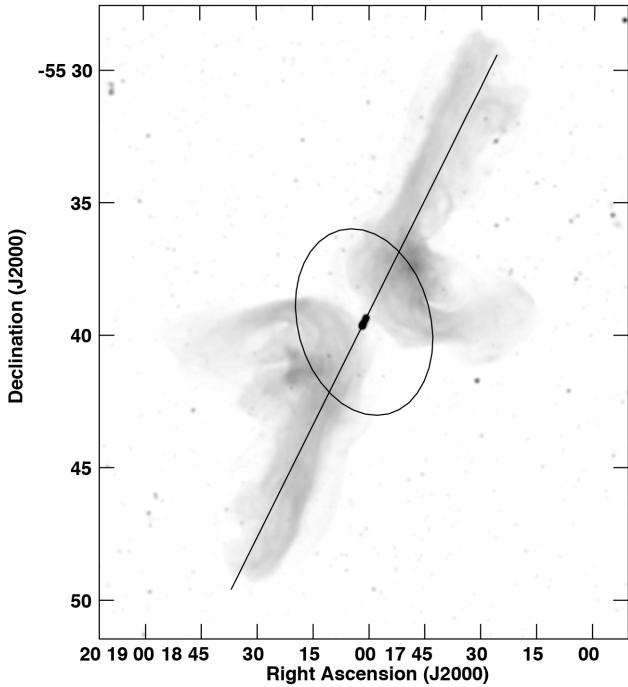**Figure 10.** The straight line segment centred on PGC 064440 is 1.57 Mpc long at the $PA = 154°$ of the line connecting the two inner radio lobes. The ISM of PGC 064440 is represented by an ellipse having an $l = 250$ kpc semimajor axis at the same $PA = 15°$ and ellipticity $\epsilon = 0.3$ as the distribution of stellar mass traced by the $K_{s}$ isophote (Table 2). The angle between the jet and the major axis of the ellipse is $\Delta = 15° + (180-154)° = 41°$.

ring, the polar axis is inclined $\approx 8°$ from the plane of the sky, with the $PA = 105°$ side closer to us and the $PA = -75°$ side farther away. Even if PGC 064440 were a thin disc, the isophotal ellipticities independently imply that its polar axis must be $\lesssim 45°$ from the plane of the sky.

Fig. 10 represents the hypothetical hot halo of PGC 064440 with an ellipse superimposed on a grey scale image of PKS 2014−55. The ellipse has the same central position, ellipticity $\epsilon \equiv (\phi_{M} - \phi_{m})/\phi_{M} = 0.3$, and major axis position angle $PA = 15°$ as the starlight of PGC 064440 traced by its outer $K_{s}$ isophote (Table 2). The shape and orientation are justified by *Chandra X-ray Observatory* images (Hodges-Kluck et al. 2010) of hot ($0.3$ keV $< kT < 2$ keV) halo gas surrounding the host galaxies of XRGs which show that the ellipticities and position angles of the hot gas follow those of the stellar light distributions.

The 1.57 Mpc long straight line in Fig. 10 is centred on PGC 064440 and has the same position angle $PA = 154°$ as the inner triple source. The fact that it closely overlaps the long arms of PKS 2014−55 proves that the radio jet orientation today is within $\sim 5°$ of its orientation when the jets were launched tens of millions of years ago and when the faint cocoons were formed even earlier. This is expected if the radio 'wings' in $PA \approx 90°$ are produced by hydrodynamical backflows from stable jets but improbable for models in which the wings are produced by changing the jet orientation.

The hydrodynamical model predicts that the ends of the wings should contain the 'oldest' synchrotron electrons. Their very steep continuum spectra (Fig. 6) are consistent with synchrotron and inverse-Compton energy losses. The cocoons are probably even older.
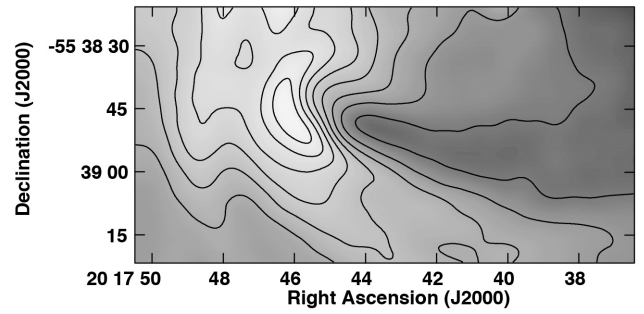


**Figure 11.** The bright bent 'head' and long dark 'tail' in this continuum image suggest blockage of the backflow by an obstacle of size $\sim 10$ kpc. The contour levels are 200 μJy beam$^{-1} \times 1, 2, 3, \ldots, 8$.

The biggest challenge to the hydrodynamical backflow model presented by PKS 2014−55 is the need to deflect both of its very wide (observed width $\sim 150$ kpc, which we treat as a cylinder of radius $r \sim 75$ kpc) backflows cleanly in opposite directions without splitting them. This requires that the hot ISM have both a high ellipticity and a large semimajor axis $l$. Capetti et al. (2002) found that XRG host galaxies in a small sample all have $\epsilon > 0.17$, a criterion easily satisfied by PGC 064440, while only three in their reference sample of 15 3C FR II galaxies have $\epsilon \geq 0.3$, the ellipticity of PGC 064440.

When they encounter the hot halo ISM of the host galaxy, backflows initially parallel to the main jets are deflected towards the most negative pressure gradient. The ellipse in Fig. 10 represents an isobaric contour, so backflows bend away from the directions in which the angle $\Delta$ between the backflow and the constant-pressure contour of the ellipse is $<90°$. For any $\Delta$, backflow radius $r$, and ellipticity $\epsilon$, this implies a minimum galaxy semimajor axis $l_{\min}$ is needed to deflect the entire backflow to one side. In the case of PGC 064440, $\Delta = 41°$ and $\epsilon = 0.3$, so $x_{i} \approx 0.854l$ and $y_{i} \approx 0.364l$. Then equation (A5) yields the minimum semimajor axis $l_{\min}$ that can cleanly deflect the backflow

$$l_{\min} = (x_{i} \sin \Delta - y_{i} \cos \Delta)^{-1} r \approx 3.5r \approx 250 \text{ kpc} , \qquad (7)$$

the size of the ellipse drawn in Fig. 10. This ellipse is just the projection of the galaxy on to the sky, which is an ellipsoid of revolution. However, the dust lane indicates that the polar axis of PGC 064440 lies only $8°$ from the plane of the sky, so the observed ellipse is a good representation of the ellipsoid.

PGC 064440 includes a stellar mass $M_{*} \approx 10^{11.6} \text{ M}_{\odot}$ (Section 4.2), so the galaxy stellar-to-halo mass relation (SHMR) predicts that its halo virial mass should be $M_{\text{vir}} \gtrsim 10^{13.3} \text{ M}_{\odot}$ (Wechsler & Tinker 2018). Such massive galaxies are typically assembled at redshift $z_{a} \sim 0.9$ and have virial radii (Shull 2014)

$$\left( \frac{R_{\text{vir}}}{206 \text{ kpc}} \right) \approx \left( \frac{M_{\text{vir}}}{10^{12} \text{M}_{\odot}} \right)^{1/3} (1 + z_{a})^{-1} . \qquad (8)$$

Thus PGC 064440 has $R_{\text{vir}} \sim 290$ kpc, and its halo is (just) big enough to completely deflect the wide backflows of PKS 2014−55.

### 5.2 Head-tail brightness features in the backflows

Radio continuum features with bright bent 'heads' and long dark 'tails' pointing downstream in the backflows (Fig. 2) of both secondary lobes at first suggest obstacles blocking the backflows. The clearest example is in the western backflow (Fig. 11), and

there are three weaker examples in the eastern backflow near J2000 $\alpha = 20^h 18^m 18\overset{s}{.}9, \delta = -55° 39' 45'', \alpha = 20^h 18^m 22\overset{s}{.}3, \delta = -55° 39' 35''$, and $\alpha = 20^h 18^m 22\overset{s}{.}3, \delta = -55° 41' 04''$. The apparent width of the dark tails is slightly larger than the $7\overset{''}{.}4$ resolution of the radio image. The corresponding linear diameter $\sim 10$ kpc is comparable with the size of cold H I discs in spiral galaxies. However, we detected no H I line emission and found no visible galaxies on the DES images downstream of the heads. Furthermore, 10 kpc is much smaller than the $2r \sim 150$ kpc diameter of the backflows. The line-of-sight depth of the backflows from such wide axially symmetric jets should be $\gg 10$ kpc, so a 10 kpc obstacle could not reduce the backflow brightness by the observed amount shown in Fig. 11, which is more than a factor of two.

The dark tail in Fig. 11 cannot be attributed to free–free absorption in an intervening ionized cloud with kinetic temperature $T \gtrsim 10^4$ K because an absorber with optical depth $\tau$ emits with brightness temperature $T_b = T[1 - \exp(-\tau)]$, and the 1.28 GHz brightness temperature $T_b \sim 2$ K of the tail implies $\tau < 10^{-3}$.

Fig. 10 shows that the dark tails appear in the downstream sides of both backflows near the deflecting halo boundary indicated by the ellipse. It also shows two matching bright regions, one just inside the apex of each 'boomerang'. These bright regions are probably not traditional FR II hotspots because they are not in the radio jets and they do not have the usual edge-brightened morphology. We suggest that the bright regions indicate compression and turbulence where backflow material is piling up inside the apex. Turbulence on scales smaller than our $\theta_{1/2} = 7\overset{''}{.}4$ beam could explain the low observed polarized intensity in the brighter northwestern region (Fig. 5). We suspect that the matched sets of dark tails are simply hydrodynamical features downstream of the bright regions, and do not actually indicate the presence of external obstructions.

## 6 SUMMARY

The hydrodynamical backflow model for PKS 2014−55 is supported by the following evidence:

(i) The observed 'double boomerang' radio morphology is expected for backflows from a pair of collinear jets redirected by the oblique hot ISM of the host galaxy. Both the magnetic fields and the total-intensity ridges follow the continuously bending flow lines. Two matching bright regions inside the boomerang apexes suggest compression and turbulence where backflow material is piling up. Bright heads and dark tails appear between both bright regions and their backflow wings. They appear to be features in the flow, not signs of obstruction by the ISM of nearby galaxies.

(ii) AGN activity in PKS 2014−55 has recently restarted (Fig. 3) with the reborn jets in the same direction (Fig. 10) as the main lobe. Thus, the secondary wings are very unlikely to be the result of a change in the orientation of the spin axis of the SMBH.

(iii) The virial halo of the host galaxy PGC 064440 is large enough and has the correct position angle to cleanly deflect backflows from the wide main jets in the direction observed.

The unique combination of high surface-brightness sensitivity ($\sigma \approx 48$ mK), high angular resolution ($\theta_{1/2} \approx 7\overset{''}{.}4$), and dense ($u$, $v$)-plane coverage of our new MeerKAT continuum image makes the very extended radio source PKS 2014−55 the best example of an XRG produced by hydrodynamical backflows from a jet with fixed orientation. The prototypical XRG NGC 326 has been cited as evidence for jet reorientation following an SMBH–SMBH merger (Merritt & Ekers 2002). However, Hardcastle et al. (2019)

reobserved the dumbbell galaxy NGC 326 with the Low-Frequency Array (LOFAR) at 144 MHz and found faint, extended radio morphological evidence for hydrodynamical effects related to an ongoing group or cluster merger. Although their result does not rule out the spin-flip model for NGC 326, we endorse their caution not to infer jet reorientation in XRGs lacking deep and detailed radio images.

The new MeerKAT continuum image also revealed faint ($T_b \sim 0.5$ K) low-pressure ($P_{min} \sim 10^{-14}$ dyne cm$^{-2}$) cocoons with sharp edges and the nearly constant brightness characteristic of subsonic (in the cocoons) expansion into the surrounding intragroup medium probed by the giant source PKS 2014−55. This pressure assumes $\kappa = 40$. The pressure in the cocoons could range from $P_{min} \sim 10^{-15}$ dyne cm$^{-2}$ if $\kappa = 0$ to $P_{min} \sim 10^{-13}$ dyne cm$^{-2}$ if $\kappa = 2000$.

## REFERENCES

Abbott T. M. C. et al., 2018, ApJS, 239, 18
Beck R., Krause M., 2005, Astron. Nachr., 326, 414
Begelman M. C., Blandford R. D., Rees M. J., 1984, Rev. Mod. Phys., 56, 255
Blandford R. D., Znajek R. L., 1977, MNRAS, 179, 433
Brentjens M. A., de Bruyn A. G., 2005, A&A, 441, 1217
Bridle A. H., Perley R. A., 1984, ARA&A, 22, 319
Bridle A. H., Hough D. H., Lonsdale C. J., Burns J. O., Laing R. A., 1994, AJ, 108, 766
Camilo F. et al., 2018, ApJ, 856, 180
Capetti A., Zamfir S., Rossi P., Bodo G., Zanni C., Massaglia S., 2002, A&A, 394, 39
Cappellari M., 2013, ApJ, 778, L2
Condon J. J., Matthews A. M., 2018, PASP, 130, 073001
Cotton W. D., 2008, PASP, 120, 439
Cotton W. D. et al., 2018, ApJ, 856, 67
Dennett-Thorpe J., Scheuer P. A. G., Laing R. A., Bridle A. H., Pooley G. G., Reich W., 2002, MNRAS, 330, 609
Ekers R. D., Fanti R., Lari C., Parma P., 1978, Nature, 276, 588
Fanaroff B. L., Riley J. M., 1974, MNRAS, 167, 31P
Fixsen D. J., Cheng E. S., Gales J. M., Mather J. C., Shafer R. A., Wright E. L., 1996, ApJ, 473, 576
Hardcastle M. J. et al., 2019, MNRAS, 488, 3416
Hindson L. et al., 2014, MNRAS, 445, 330

Hodges-Kluck E. J., Reynolds C. S., Cheung C. C., Miller M. C., 2010, ApJ, 710, 1205

Ishwara-Chandra C. H., Saikia D. J., 1999, MNRAS, 309, 100

Jarrett T. H. et al., 2011, ApJ, 735, 112

Jonas J. et al., 2016, in Taylor R. et al., eds, Proc. Sci., The MeerKAT Radio Telescope. SISSA, Trieste, PoS(MeerKAT2016)001

Jones D. H. et al., 2009, MNRAS, 399, 683

Joshi R. et al., 2019, ApJ, 887, 266

Klein U., Mack K.-H., Gregorini L., Parma P., 1995, A&A, 303, 427

Kochanek C. S. et al., 2001, ApJ, 560, 566

Lal D. V., Rao A. P., 2005, MNRAS, 356, 232

Leahy J. P., Williams A. G., 1984, MNRAS, 210, 929

Ledlow M. J., Owen F. N., 1996, AJ, 112, 9

Malarecki J. M., Staveley-Smith L., Saripalli L., Subrahmanyan R., Jones D. H., Duffy A. R., Rioja M., 2013, MNRAS, 432, 200

Malarecki J. M., Jones D. H., Saripalli L., Staveley-Smith L., Subrahmanyan R., 2015, MNRAS, 449, 955

Mauch T., Murphy T., Buttery H. J., Curran J., Hunstead R. W., Piestrzynski B., Robertson J. G., Sadler E. M., 2003, MNRAS, 342, 1117

Mauch T. et al., 2020, ApJ, 888, 61

McMullin J. P., Waters B., Schiebel D., Young W., Golap K., 2007, ASP Conf. Ser. Vol. 376, Astronomical Data Analysis Software and Systems XVI. Astron. Soc. Pac., San Francisco, p. 127

Merritt D., Ekers R. D., 2002, Science, 297, 1310

Pacholczyk A. G., 1970, Radio astrophysics. Nonthermal Processes in Galactic and Extragalactic Sources. W. H. Freeman and Company, San Francisco

Panessa F. et al., 2016, MNRAS, 461, 3153

Paturel G., Fouque P., Bottinelli L., Gouguenheim L., 1989, A&AS, 80, 299

Reynolds J. E., 1994, ATNF Memo, AT/39.3/040

Saripalli L., Subrahmanyan R., 2009, ApJ, 695, 156

Saripalli L., Subrahmanyan R., Laskar T., Koekemoer A., 2008, Proc. Sci., 052, 130

Shull J. M., 2014, ApJ, 784, 142

Simpson C., Ward M., Clements D. L., Rawlings S., 1996, MNRAS, 281, 509

Skrutskie M. F. et al., 2006, AJ, 131, 1163

Stocke J. T., Keeney B. A., Danforth C. W., Oppenheimer B. D., Pratt C. T., Berlind A. A., Impey C., Jannuzi B., 2019, ApJS, 240, 15

Tadhunter C. N., Fosbury R. A. E., Quinn P. J., 1989, MNRAS, 240, 225

Wechsler R. H., Tinker J. L., 2018, ARA&A, 56, 435

Willis A. G., Strom R. G., Wilson A. S., 1974, Nature, 250, 625

Worrall D. M., Birkinshaw M., 2006, Multiwavelength Evidence of the Physical Processes in Radio Jets, Lect. Notes Phys. 693. Springer-Verlag Berlin Heidelberg, New York, p. 39

Worrall D. M., Birkinshaw M., Cameron R. A., 1995, ApJ, 449, 93

Wright A., Otrupcek R., 1990, PKS Catalog, Australia Telescope National Facillity. Epping, NSW, Australia

Wright E. L. et al., 2010, AJ, 140, 1868

## APPENDIX: MINIMUM SIZE OF THE DEFLECTING HALO

In the coordinate system with $x$ parallel to the major axis and $y$ parallel to the minor axis, the equation of the deflecting ellipse with semimajor axis $l$ and ellipticity $\epsilon$ is

$$x^2 + \left(\frac{y}{1-\epsilon}\right)^2 = l^2 \tag{A1}$$

and tangents to the ellipse have slopes

$$\frac{\mathrm{d}y}{\mathrm{d}x} = -(1-\epsilon)^2 \frac{x}{y} . \tag{A2}$$

If $\Delta$ is the angle between the backflow and the $x$ axis, the equation of the outermost backflow of radius $r$ is

$$y = x \tan \Delta - \frac{r}{\cos \Delta} \tag{A3}$$

and the initial slope of the backflow is $\tan \Delta$. At the point $(x_i, y_i)$ where it intersects the ellipse at a 90° angle, the slope of the ellipse is $-(\tan \Delta)^{-1}$ and

$$\frac{y_i}{x_i} = (1-\epsilon)^2 \tan \Delta . \tag{A4}$$

The point $(x_i, y_i)$ must also satisfy equation (A1) so

$$x_i = l[1 + (1-\epsilon)^2 \tan^2 \Delta]^{-1/2} . \tag{A5}$$

This paper has been typeset from a TEX/LATEX file prepared by the author.